Synchronised multi-scale image analysis of soil deformations

Yining Teng BEng
Research Student, Centre for Offshore Foundation Systems, University of Western Australia, Crawley, WA, Australia

Samuel A. Stanier MEng, PhD
Research Fellow, Centre for Offshore Foundation Systems, University of Western Australia, Crawley, WA, Australia (corresponding author: sam.stanier@uwa.edu.au)

Susan M. Gourvenec BEng, PhD
Professor, Centre for Offshore Foundation Systems, University of Western Australia, Crawley, WA, Australia

New apparatus and techniques for performing synchronised multi-scale particle image velocimetry or digital image correlation (PIV/DIC) soil deformation measurements have been developed. A central camera records a full field of view (FoV) of the model capturing the 'macro' deformation mechanism and the boundaries of the model. Simultaneously, an adjacent slave camera records a subset of the full FoV capturing the 'micro' soil response in a region of special interest, such as under the corner of footing. The 'micro' FoV images have higher resolution in terms of particle/pixel size ratio (d/p), resulting in the ability to measure localised deformations that are invisible to lower resolution images. Recommendations are made with respect to appropriate subset size and spacing for high-resolution images. A photogrammetric correction process requiring a small number of static control points is proposed and the performance is validated against a conventional photogrammetric calibration utilising a large array of static control points. Lastly, results from a validation experiment are presented comparing the PIV/DIC output from the 'macro' and 'micro' FoV, illustrating that: (*a*) the photogrammetric correction method proposed is robust and (*b*) that there has been an improvement in spatial resolution of the strain measurements that can be obtained through the 'micro' FoV camera.

Notation

B	footing width	p	pixel
CC_{ZNCC}	zero normalised cross-correlation coefficient	p_1	tangential lens distortion parameter
$CC_{ZNCC\text{-}min\text{-}tol}$	full-field correlation coefficient tolerance	p_2	tangential lens distortion parameter
$CC_{ZNCC\text{-}seed\text{-}tol}$	seed correlation coefficient tolerance	r	radius
c	initial coordinates of the subset	s	subset spacing
c'	final coordinates of the subset	t_x	translation magnitude
D_s	diameter of GeoPIV-RG subset	t_y	translation magnitude
D_x	width of a pixel on the camera sensor in object space units	t_z	translation magnitude
D_y	height of a pixel on the camera sensor in object space units	u	horizontal displacement in image space
		v	vertical displacement in image space
		X	horizontal position in object space units
d	particle diameter	x	horizontal position in image space
d_{50}	median particle diameter	x_0	horizontal position of the principal point of camera in image space
E	initial strain element centroid	$\tilde{x}$	horizontal position in camera sensor space *w.* central origin
E'	final strain element centroid	Y	vertical position in object space units
f	camera focal length	y	vertical position in image space
k_1	radial lens distortion parameter	y_0	vertical position of the principal point of camera in image space
k_2	radial lens distortion parameter		
L	gauge length	$\tilde{y}$	vertical position in camera sensor space *w.* central origin
$M40$	40-pixel diameter subset in 'macro' view		
max_{iter}	maximum number of iterations per subset	α	pixel non-squareness ratio

53

International Journal of Physical Modelling in Geotechnics
Volume 17 Issue 1

Synchronised multi-scale image analysis
of soil deformations
Teng, Stanier and Gourvenec

$\|\Delta \boldsymbol{p}\|_{\max}$	maximum norm of the shape function difference vector
$\delta_{\tilde{x}:\mathrm{r}}$	horizontal error due to radial lens distortion
$\delta_{\tilde{x}:\mathrm{t}}$	horizontal error due to tangential lens distortion
$\delta_{\tilde{y}:\mathrm{r}}$	vertical error due to radial lens distortion
$\delta_{\tilde{y}:\mathrm{t}}$	vertical error due to tangential lens distortion
κ	Euler rotation angle between the N axis and the X axis
μ	coordinate scale factor
$\mu 70$	70-pixel diameter subset in 'micro' view
$\mu 180$	180-pixel diameter subset in 'micro' view
$\sigma_{I_{\mathrm{s}}}$	standard deviation of subset pixel intensities
ϕ	Euler rotation angle between the Z' axis and the Z axis
ω	Euler rotation angle between the X' axis and the N axis

1. Introduction

This paper presents a new synchronised multi-scale image analysis apparatus for observing soil deformations in a geotechnical centrifuge using particle image velocimetry (PIV – also known as digital image correlation or DIC). The system is an extension of that described by Stanier and White (2013), which used a small form factor machine vision camera and bespoke software to provide in-flight live view of the images captured at rates of up to 15 frames/s. An additional camera was added to this system to enable synchronised images of two fields of view (FoV) to be captured simultaneously: one of the whole domain or the so-called 'macro' FoV and the other focusing on a smaller specific region of interest (RoI), the so-called 'micro' FoV. The 'micro' view images are of significantly higher resolution in terms of particle/pixel size ratio (d/p) allowing localised deformations to be measured that are invisible to lower resolution images. Visualising soil behaviour at the 'micro' scale, as well as at the 'macro' scale, to identify macroscopic failure mechanisms, provides much stronger experimental support for geotechnical analysis, and in particular the development of complex constitutive or discrete-element models.

2. Background

PIV techniques (Adrian, 1991; Westerweel, 1997) and DIC techniques (Sutton et al., 1983, 2000) have been widely used for measuring deformation fields in physical modelling tests. Over the past 15 years, PIV/DIC techniques have been developed specifically for geotechnical applications (e.g. Hall, 2012; Iskander, 2010; Omidvar et al., 2014; Rechenmacher and Finno, 2004; Stanier et al., 2015; Take, 2015; White et al., 2001, 2003). These techniques have been used to observe the macro failure mechanisms of many different geostructures,

including, for example: pipelines (Dingle et al., 2008), shallow foundations (Mana et al., 2012), jack-up foundations during punch through (Hu et al., 2014), fault rupture propagation in slopes (Anastasopoulos et al., 2007), slope failure due to seasonal wetting and drying (Take and Bolton, 2011), settlements due to tunnelling in sand (Marshall et al., 2012) and helical screw piles (Stanier et al., 2013). All of the above examples include PIV/DIC-facilitated observations of the macro response of the soil around the geostructures, in some cases with comparison to numerical and/or simple analytical models approximating the mechanisms.

In modern PIV/DIC algorithms (e.g. Blaber et al., 2015; Pan et al., 2010; Stanier et al., 2015), displacements are generally obtained by

(a) discretising the RoI within a 'reference' image with a mesh of subsets at a regular spacing interval
(b) for each subset
  (i) calculating a measure of cross-correlation (e.g. normalised cross-correlation (NCC); Lewis, 1995) between the 'reference' image and all integer pixel locations within the RoI in the 'target' image
  (ii) obtaining an initial estimate of the displacement of the subset (u, v) by locating the peak in the cross-correlation map
  (iii) refining the displacements (u, v) to subpixel resolution using a subset shape function to describe the deformation within the subset, achieved by finding optimal values for the subset shape function parameters using an iterative technique (e.g. the inverse-compositional Gauss–Newton (IC-GN) method; Pan et al., 2010) and image intensity interpolation (e.g. bi-quintic b-spline; Cheng et al., 2002). A first-order subset shape function with deformation parameters describing the displacements (u, v) and the displacement gradients ($\partial u/\partial x$, $\partial v/\partial y$, $\partial u/\partial y$ and $\partial v/\partial x$) (Stanier et al., 2015) is applied.

The above measurement process relies on the assumption that the fraction of FoV within the subset deforms continuously and that the order of that deformation is matched by the order of the subset shape function (Stanier et al., 2016). In many experimental mechanics applications of PIV/DIC – such as inferring material properties from full-field displacements (Avril et al., 2008) – the deformations observed are typically small and strain localisations tend not to occur except perhaps at the very end of a test. However, in geotechnical models displacements, rotations and deformations are often significantly larger – especially close to the geostructure – making an accurate measurement of soil displacements more onerous

International Journal of Physical Modelling in Geotechnics
Volume 17 Issue 1

**Synchronised multi-scale image analysis
of soil deformations**
Teng, Stanier and Gourvenec

(Figure 1). There is also the potential for localisation of deformations within the body of soil, resulting in high gradients of deformation, at all stages of the experiment.

For granular materials, such as sand, the size of these localisations has been estimated to be of the order of $\sim 10d_{50}$ (Muir Wood, 2012). It has been established that the images used in the PIV/DIC analysis of granular deformation must have image resolution in terms of the particle/pixel size ratio (d/p) of >4 to avoid bias errors and peak locking (Stanier *et al.*, 2016). This makes the approximate size of a potential localisation in granular materials ~ 40 pixels for images with moderate resolution ($d/p \approx 4$), which is typical of the size of subsets generally used in geotechnical PIV/DIC analyses. In this scenario, many subsets are likely to straddle any localisation features that occur, leading to the subset shape function becoming 'undermatched', that is, unable to approximate the deformation within the subset resulting in rapid decorrelation and

bias errors (or drift) in displacement measurements (Schreier and Sutton, 2002). Much higher resolution images (i.e. $d/p \gg 4$) are likely to be required to measure the deformation occurring within the localisations that occur in granular assemblies.

This paper first describes the hardware and software required to obtain synchronous multi-scale PIV/DIC measurements at moderate and high resolution ($d/p = 4$ and 18, respectively). Guidance is then provided on appropriate choices for subset size and spacing with key pitfalls of choosing inappropriate analysis parameters highlighted through examples. A modified photogrammetric correction process to convert the image space (pixel) measurements to model units (mm) – requiring only a small number of static control points – is then proposed and validated. Lastly, experimental data is used to demonstrate the improved resolution of strain field that can be observed using the synchronous multi-scale apparatus.
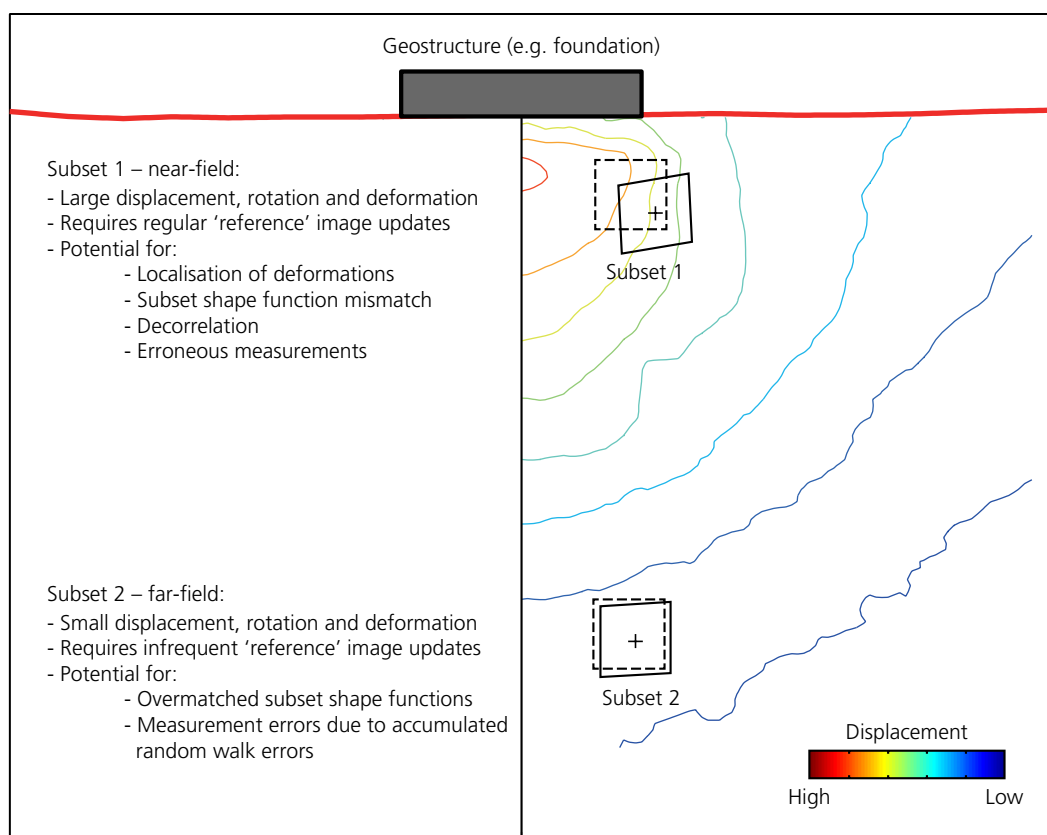
Figure 1. Schematic diagram of a typical geotechnical model test incorporating PIV/DIC measurements illustrating the range of subset displacements, rotations and deformation experienced across the FoV of the digital camera

International Journal of Physical Modelling in Geotechnics
Volume 17 Issue 1

Synchronised multi-scale image analysis
of soil deformations
Teng, Stanier and Gourvenec

3. Apparatus

3.1 Hardware

The new synchronised multi-scale image capture system requires minimal additional hardware compared with conventional geotechnical PIV/DIC, requiring only a second camera and control unit that can synchronously trigger both cameras. The multi-scale system hardware is shown in Figure 2. It is a further development on the system described by Stanier and White (2013) and comprises the following components.

- Centrifuge strongbox – housing the cameras, lighting and soil sample within the PIV strongbox.
- PIV/DIC strongbox – a strongbox that fits within the main centrifuge strongbox that contains the soil sample. A transparent acrylic window is provided to expose a plane of the soil sample allowing digital images to be captured. Arrays of control markers are pre-installed within the window to provide control points with known model space locations for photogrammetric correction of measurements.
- Cameras – two 5-megapixel cameras (Allied Vision Technologies Prosilica GC2450C) with charge-coupled device (CCD) sensors and Gigabit Ethernet connectivity. These cameras have a maximum frame rate of 15 frames/s at full resolution. The master camera (viewing the whole, i.e. 'macro' FoV) has an 8 mm lens positioned at the centre of the experimental set-up. The slave camera (viewing a subset of the model, the 'micro' FoV) has a 43 mm

lens and is positioned adjacent to the master camera. The 8 and 43 mm focal lengths were appropriate for the centrifuge PIV strongbox set-up used in the beam centrifuge at the University of Western Australia (UWA). Different focal lengths may be required for other experimental set-ups.

- Power supply – an in-house 60 V electric power supply is used to support the operation of the cameras and light-emitting diode (LED) panels (not shown in Figure 2 but typically attached to the swing arm of the centrifuge).
- Control units – two control units control the activities of the two cameras. Each unit is connected to a camera and controls the exposure time and frame capture rate. The two control units are connected using an additional cable so that triggering of the two cameras is synchronous, with the 'slave' camera duplicating the activity of the 'master' camera. The controllers also incorporate an LED control unit (Gardasoft RT220) with a local area network (LAN) interface allowing a transmission control protocol/internet protocol (TCP/IP) link to control the brightness of LED panels independently (Stanier and White, 2013).
- Lighting – a pair of LED panels (CCS Industries Ltd, model number LDL2-266X30SW-WD) are positioned near the top of the centrifuge strongbox. Light intensity and lighting position can be adjusted to achieve bright and even lighting on the whole FoV using the aforementioned control units.
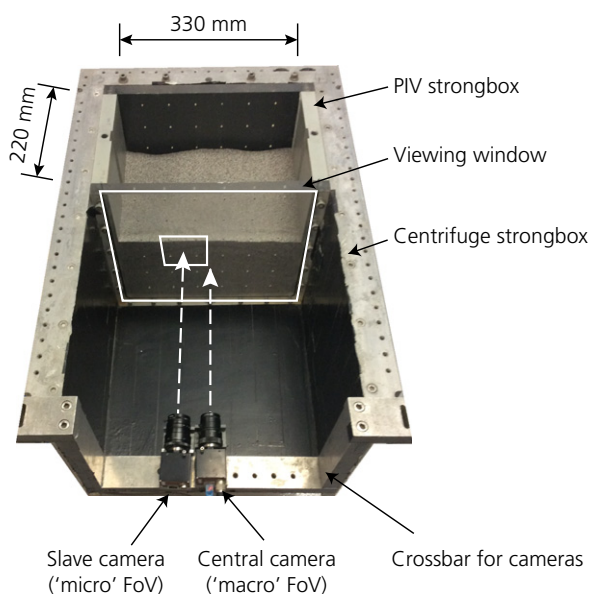
3.2 Software

The multi-scale PIV/DIC system is controlled by an extension of the software described by Stanier and White (2013). Specifically, the software consists of two packages, written and compiled in the National Instruments LabVIEW environment.

(a) DigiCAM – In-house image capturing software. Controls exposure times and frame capture rate while providing live video of the camera view. The two cameras are controlled by duplicate interfaces. One instance of the software runs in master mode and controls the 'macro' view camera, while a second runs in slave mode, assimilating the various settings directly from the master camera.

(b) DigiLED – Software to control the light intensity of each of the LED panels to generate even illumination of the model.

Post-processing of the images captured using the two cameras was conducted using the following MATLAB software.

- GeoPIV-RG (available for free download at http://www. geopivrg.com) – PIV/DIC image analysis software incorporating a first-order subset shape function, bi-quintic b-spline image intensity interpolation and IC-GN subset

Figure 2. Synchronous multi-scale PIV/DIC apparatus developed for the UWA beam centrifuge

330 mm
220 mm

PIV strongbox
Viewing window
Centrifuge strongbox

Slave camera ('micro' FoV)   Central camera ('macro' FoV)   Crossbar for cameras

International Journal of Physical Modelling in Geotechnics
Volume 17 Issue 1

**Synchronised multi-scale image analysis
of soil deformations**
Teng, Stanier and Gourvenec

deformation parameter optimisation. This algorithm provides at least an order of magnitude improvement in measurement precision compared with the PIV/DIC approaches most commonly used in geotechnical applications (Stanier *et al.*, 2015).

■ GeoCALIBRATE_RG_micro – A modified camera calibration script developed to convert pixel measurements derived from images recorded by the slave ('micro' view) camera to model scale units (e.g. mm). Conventional camera calibration techniques (White *et al.*, 2003) are not applicable for the slave camera due to the very few control points being visible in the images recorded, as discussed in detail later in this paper. This newly developed subroutine is available to the geotechnical research community for free download at http://www.geopivrg.com.

4. Effect of system on image texture

To demonstrate the impact of the higher resolution 'micro' view on the subset texture quality, a physical model test involving vertical penetration of a 50 mm width (B), 220 mm length (L), 10 mm thick strip foundation was performed on silica sand. The test was performed in the beam centrifuge at UWA under acceleration at the sample surface of 50g. The experimental set-up is shown in Figure 2. The 'macro' view camera captures images of an FoV of $\sim 350 \times 300$ mm while the 'micro' view camera captures images of an FoV of $\sim 80 \times 60$ mm. The 5 megapixels (2448×2050 pixels) yield images with pixel density per object unit area of 1045·5 and 47·8 p/mm^2 for the 'micro' and 'macro' view images, respectively – that is, a factor of ~ 20 difference in resolution.

The soil sample within the strongbox consisted of ~ 180 mm depth of UWA medium-coarse silica sand (d_{50} of 510 μm). The combination of the d_{50} of the sand and the FoV of the 'macro' and 'micro' view cameras yield d_{50}/p ratios of ~ 4 and ~ 18, respectively. This is sufficient to avoid significant 'peak-locking' errors and associated strain field bias errors in the 'macro' view images (Stanier *et al.*, 2016). For the 'micro' FoV, assuming that potential deformation localisations are of the order of $10d_{50}$ in size (Muir Wood, 2012), and that a subset 40 pixels in size contains sufficient information for accurate cross-correlation, the analysis subsets will be $\sim 20\%$ of the size of any localisation features. This potentially allows subsets to populate any localisation features without suffering from excessive decorrelation due to 'under-matching' of the subset shape function.

The sand sample was dry pluviated to a relative density of 70%. Prior to pluviation, a fraction of the sand was dyed black and mixed uniformly with undyed sand to enhance the contrast between the neighbouring particles. Optimal contrast was achieved by following the procedure recommended by Stanier
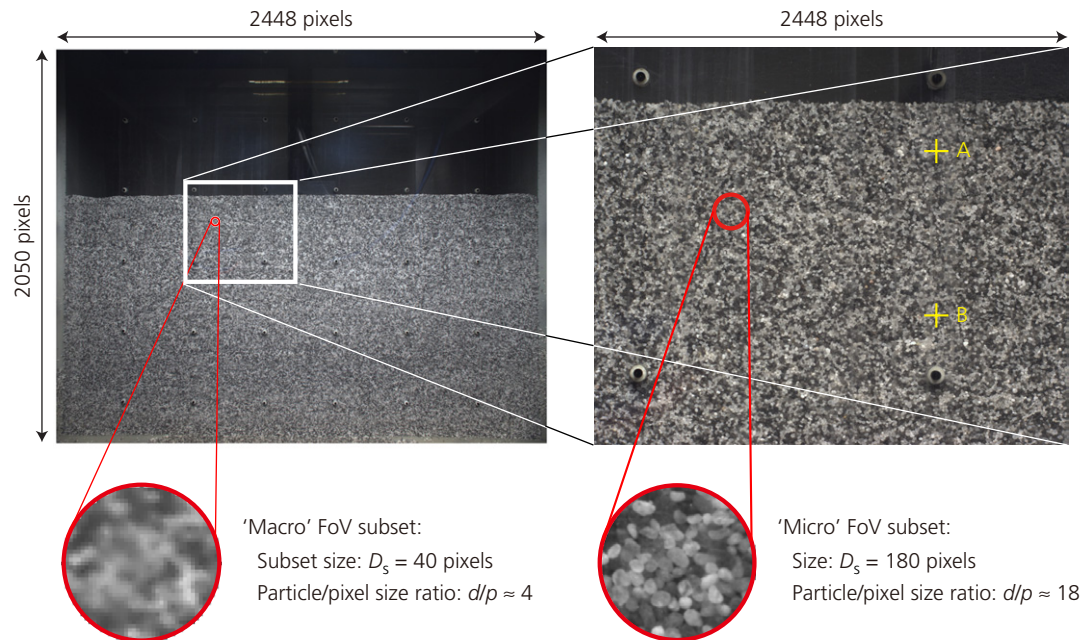
and White (2013) such that the artificial seeding ratio was ~ 0.5. Images were captured during ramp-up, penetration testing and ramp-down. During the experiment the footing was penetrated into the soil at a rate of 0·1 mm/s to a depth of 6·7 mm; hence, in this instance the total penetration depth was smaller than the thickness of the foundation. In total, 336 images were captured during the footing penetration by each camera at a frequency of 5 Hz.

### 4.1 Subset size and texture quality

Figure 3 shows the difference in resolution for 'macro' and 'micro' view images for subsets of equivalent model space dimensions (40-pixel diameter in the 'macro' view and 180-pixel diameter in the 'micro' view) noting that circular subsets are utilised in GeoPIV-RG to reduce the potential for measurement bias emanating from subset shape function mismatch. A subset diameter of 40 pixels was chosen for the 'macro' view images, as the subset then contains ~ 100 sand particles, which should provide sufficient information within each subset for accurate cross-correlation (Stanier *et al.*, 2016). The two subsets, represented by red circles in Figure 3, capture the same surface area of the model in the same location. Individual sand particles can be clearly distinguished in the 'micro' view subset, while a similar detail is not discernible in the 'macro' view subset.

To provide a comprehensive analysis of the impact of the 'micro' view on subset texture quality, two subset texture quality parameters have been calculated: (*a*) the standard deviation of subset pixel intensities (σ_{I_s}) (Stanier and White, 2013) and (*b*) the sum of the square of subset intensity gradients (SSSIG) (Pan *et al.*, 2008). The former is a simple measure of the contrast within the subset with values of $\sigma_{I_s} > 15$ indicating adequate contrast (Stanier and White, 2013) while the latter is a measure of the distribution of the contrast with values of SSSIG $> 10^5$ indicating adequate texture distribution (Pan *et al.*, 2008). These measures have been calculated for a range of subsets of varying diameter but of the same object space locations (i.e. subset centroid location) for the 'micro' view at two locations. These measures are compared with those for 40-pixel diameter subsets at the same object space locations for the 'macro' view in Figure 4. Red lines mark the adequate subset texture quality thresholds referred to above.

The 40-pixel diameter 'macro' view subsets satisfy both criteria at both the locations analysed. For the 'micro' view images, subset diameters > 70 pixels also satisfy the criteria at both the locations analysed. In general, an appropriately sized subset for image analysis of geotechnical problems should be one that is sufficiently large to contain adequate information for reliable cross-correlation, while also being small enough that the shape function adequately captures the deformation within the subset

International Journal of Physical Modelling in Geotechnics
Volume 17 Issue 1

**Synchronised multi-scale image analysis
of soil deformations**
Teng, Stanier and Gourvenec

Figure 3. Example images captured using the 'macro' (left hand side) and 'micro' (right hand side) FoVs with magnified view of example subsets to illustrate the difference in image resolution
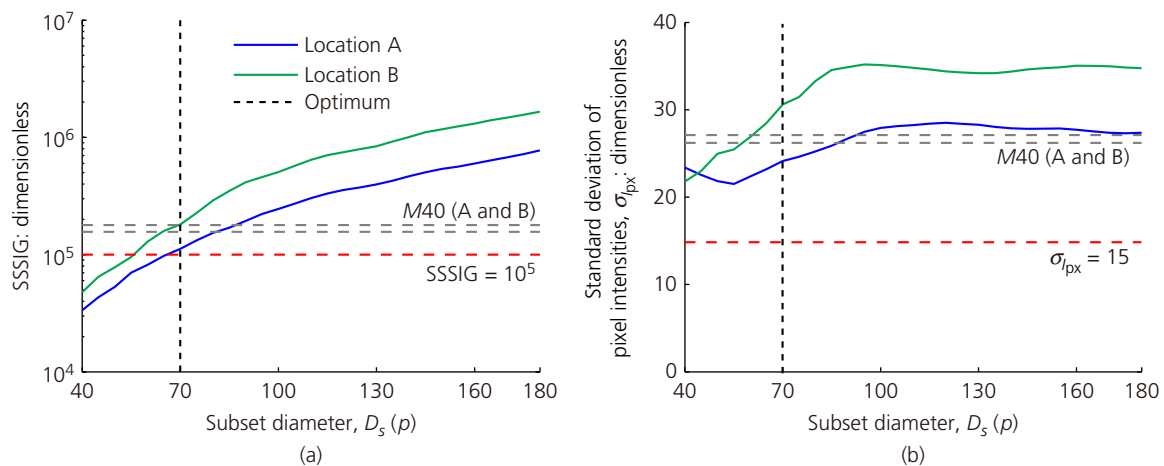
Figure 4. Measures of subset quality for a range of subset diameters for the 'micro' FoV compared with 40-pixel diameter subset for the 'macro' view: (a) standard deviation of pixel intensities ($\sigma_{I_{px}}$); and (b) SSSIG

(Stanier *et al.*, 2016). Therefore, a subset size of 70 pixels was deemed optimal for the 'micro' view images as it is the smallest size subset for which there is adequate information within the signal for reliable cross-correlation.

4.2 Subset size and correlation quality

The zero-normalised cross-correlation coefficient (CC_{ZNCC}) is a robust measure of subset correlation quality that is invariant to global changes in illumination (Pan *et al.*, 2010),

58

International Journal of Physical Modelling in Geotechnics
Volume 17 Issue 1

Synchronised multi-scale image analysis
of soil deformations
Teng, Stanier and Gourvenec

with values of 0 and 1 intuitively indicating zero and perfect correlation, respectively. It is calculated as

1. $$CC_{ZNCC} = \frac{\sum_{i,j \in n_s} \left(I_{ij}^{r} - \bar{I}^{r}\right)\left(I_{ij}^{t} - \bar{I}^{t}\right)}{\sqrt{\sum_{i,j \in n_s}\left[I_{ij}^{r} - \bar{I}^{r}\right]^2 \sum_{i,j \in n_s}\left[I_{ij}^{t} - \bar{I}^{t}\right]^2}}$$

where I_{ij}^{r} and I_{ij}^{t} are the pixel intensities for a given i, j coordinate in the 'reference' and 'target' images, respectively. The mean pixel intensities for the 'reference' and 'target' images are calculated as

2. $$\bar{I}^{r} = \frac{1}{n_s}\sum_{i,j \in n_s} I_{i,j}^{r}; \quad \bar{I}^{t} = \frac{1}{n_s}\sum_{i,j \in n_s} I_{i,j}^{t}$$

where n_s is the number of pixels in the subset.

The efficacy of the PIV/DIC displacement measurement technique relies on the assumption that the deformation within the subset is continuous and of the same order as the shape function used to model the deformation within it, so that the measure of cross-correlation defined in Equation 1 can remain close to unity. For granular materials such as sands, any discontinuous deformation (typically caused by particle rearrangement) occurring within a subset results in decorrelation (indicated by a reduction in CC_{ZNCC}) due to the subset shape function becoming 'under-matched'. If the decorrelation becomes excessive (i.e. CC_{ZNCC} falls below a user-defined tolerance, $CC_{ZNCC\text{-}tol}$) the 'reference' image must be updated so as to regain adequate cross-correlation quality.

The zero NCC coefficient (CC_{ZNCC}) was calculated throughout the footing penetration test using GeoPIV-RG for subsets at locations A and B (Figure 3) of 40-pixel diameter ($M40$) in the 'macro' view and 180- and 70-pixel diameters ($\mu180$ and $\mu70$) in the 'micro' view. $CC_{ZNCC\text{-}tol}$ was specified as 0·75, the maximum number of iterations of the IC-GN optimisation of the deformation parameters for the subset shape function (max_{iter}) was set to 50 and the maximum difference of the norm of the shape function difference vector ($|\Delta p|_{\text{max}}$) was set to 1×10^{-5}, following the recommendations in Stanier et al. (2015).

Figures 5(a) and 5(d) indicate that the decorrelation of the $M40$ subsets at locations A and B was moderate and thus the 'reference' image did not require updating. However, Figures 5(b) and 5(e) show that the $\mu180$ subset used in the analyses of the 'micro' view images suffered from significant decorrelation. The very sudden decorrelation prior to 'reference' image updating at locations A and B is indicative of the subset shape function becoming 'under-matched'. That these

subsets are of equivalent object space size and utilise the same order subset shape function illustrates that the 'micro' view images must contain additional information about the deformations occurring within the subsets that is not captured in the lower resolution 'macro' view images.
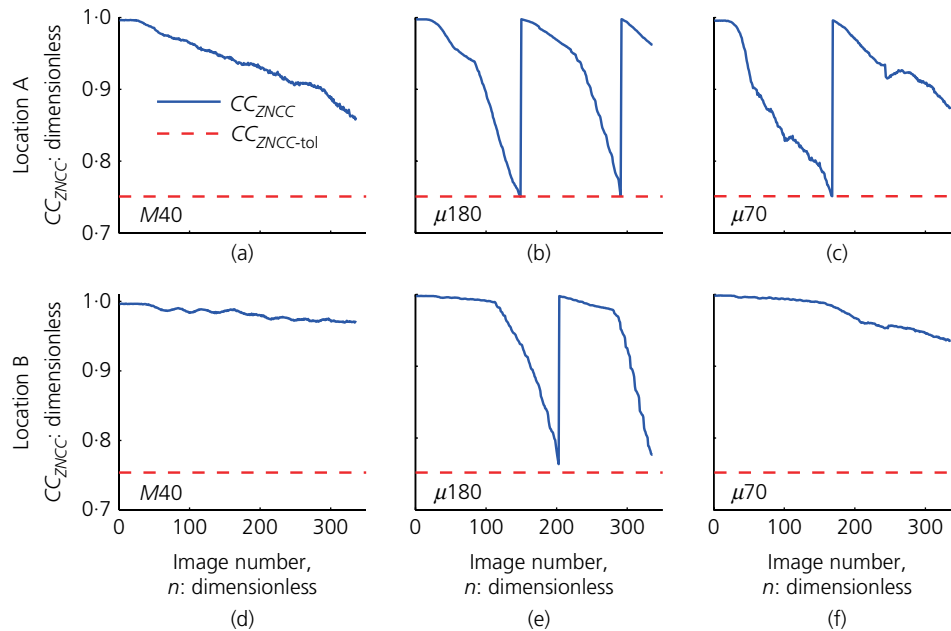
Figure 4 shows that the $\mu180$ was potentially larger than necessary as the σ_{I_s} and the SSSIG are both greater than the recommended quality thresholds (Pan et al., 2008; Stanier and White, 2013; Stanier et al., 2016). Figures 5(c) and 5(f) illustrate that smaller subsets ($\mu70$) can be used to better analyse the 'micro' images, as the 'reference' image required updating less frequently due to the subset shape function being able to better match the deformations. The correlation coefficients are generally lower for the smaller subset, as for a given d/p ratio, any particle rearrangement has a proportionally greater effect on the correlation coefficient. Nonetheless, despite the enhanced sensitivity to particle rearrangement, there is no evidence of 'under-matched' subset shape function errors. On the basis of the above observations, the smallest subset with suitable subset quality measures ($\sigma_{I_s} > 15$ and SSSIG $> 1 \times 10^5$) is recommended for the analysis of high-resolution images, so as to

(a) minimise the potential for errors due to the subset shape function being 'under-matched' (the effect of under-matching on strain measurements is demonstrated later in this paper)

(b) ensure that the subset is comfortably smaller than the size of any localisation feature anticipated to develop within the model (i.e. D_s (mm) $\ll 10d_{50}$).

4.3 The effect of subset size and spacing on strain measurement

Figure 6 is an illustration of how triplets of subsets (located initially at coordinates c_1, c_2 and c_3 and finally at c_1', c_2' and c_3'), separated by element length L, are typically used to calculate measures of strain at the centroid of the triplet (located initially at E and finally at E') using their displacements ($c_1 - c_1'$, $c_2 - c_2'$ and $c_3 - c_3'$). To explore the effect that subset size and spacing has on strain measurements, triplets of subsets were placed in an equilateral triangle with centroids at locations A and B (Figure 3) and varying element length L. The trajectories of these triplets of subsets were then computed using GeoPIV-RG adopting the same analysis settings as previously, following which the shear (γ) and volumetric strains (ε_v) were calculated following White and Bolton (2004).

Figures 7(a), 7(d), 8(a) and 8(d) indicate that the element length L has only a minor effect on the measured shear and volumetric strains for the 'macro' view analysis ($M40$). This demonstrates that the measurements are unaffected by bias due

International Journal of Physical Modelling in Geotechnics
Volume 17 Issue 1

Synchronised multi-scale image analysis
of soil deformations
Teng, Stanier and Gourvenec

Figure 5. Decorrelation for subset locations A and B for: (a, d) 40-pixel 'macro' view subset ($M40$); (b, e) 180-pixel 'micro' view subset ($\mu180$); and (c, f) 70-pixel 'micro' view subset ($\mu70$)
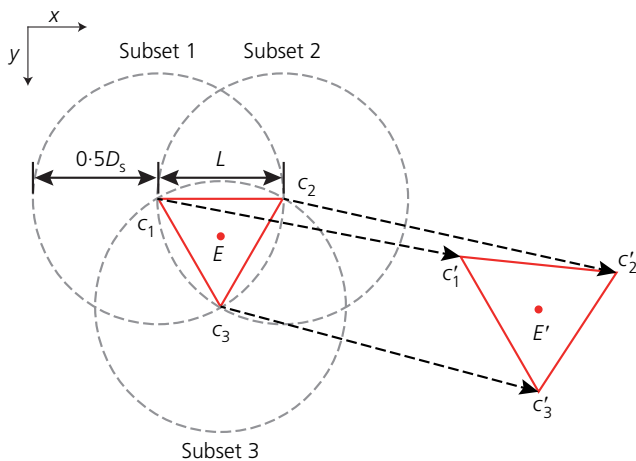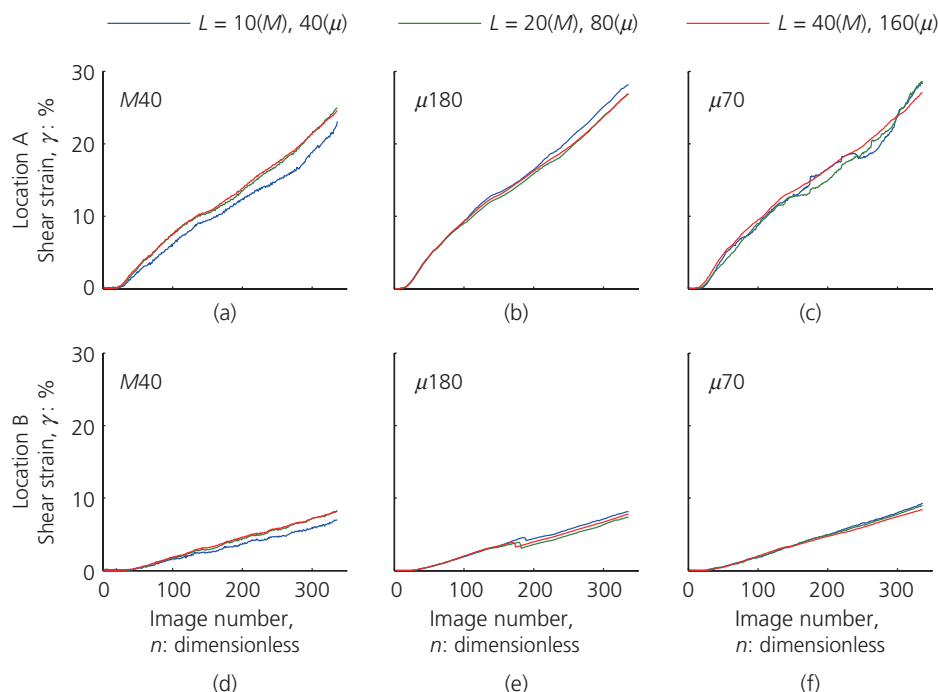

Figure 6. Schematic diagram of strain element geometry with centroid located at E and E' comprising of a triangle of subsets with centroids located at c_1, c_2, c_3, c'_1, c'_2 and c'_3

to 'peak locking' (Stanier *et al*., 2016). Figures 7(b), 7(e), 8(b) and 8(e) show that the equivalently sized (in model space terms) 'micro' view analysis ($\mu180$) is in general agreement with the 'macro' view analysis with respect to the magnitude

of the strains measured, irrespective of the element length L. However, there is a clear drift in shear and volumetric strains at location B, which is caused by the subset shape function becoming 'under-matched' at approximately the same strain magnitudes for all L. Figures 7(c), 7(f), 8(c) and 8(f) show that reducing the subset size to 70 pixels in the 'micro' view ($\mu70$) results in very similar shear strain measurements as for the larger subset ($\mu180$). However, the volumetric strains – particularly at location A – vary significantly with element length L, indicating that the use of smaller subsets and closer spacing (leading to increased measurement density) leads to the measurement of dilation that is masked in the 'macro' view images due to their lower resolution (in terms of d/p ratio), and in the 'micro' view analysis utilising the large subset ($\mu180$) due to the subset shape function becoming 'under-matched'.

Figure 9(a) shows the shear strain drift for the large subset ($\mu180$) used to compute the shear strain for an element at location B, where L was 160 pixels. The calculated displacement of subset number 2 drifts erroneously immediately prior to the 'reference' image being updated (Figures 9(c) and 9(d)), which is a result of the subset shape function becoming 'under-matched' as indicated by the corresponding rapid fall in CC_{ZNCC} (Figure 9(b)). Therefore, it is important to use the smallest subset size exhibiting adequate image texture quality

60

International Journal of Physical Modelling in Geotechnics
Volume 17 Issue 1

**Synchronised multi-scale image analysis
of soil deformations**
Teng, Stanier and Gourvenec

Figure 7. Shear strain (γ) measured using triangular elements of varying element length L at locations A and B for: (a, d) 40-pixel diameter subset in 'macro' view (M40); (b, e) 180-pixel diameter subset in 'micro' view (μ180); and (c, f) 70-pixel diameter subset in 'micro' view (μ70)

($\sigma_{I_s} > 15$ and $\mathrm{SSSIG} > 1 \times 10^5$) to reduce the potential for the subset shape function becoming 'under-matched' and to explore carefully the effect of subset spacing on the resulting analysis to minimise the potential of bias errors polluting the strain measurements.

5. Photogrammetric correction

5.1 Background

It is generally preferable for model measurements made using digital images to be converted from image space units (pixels) to more meaningful object space units (e.g. mm). Digital imaging systems typically consist of a small planar sensor (or CCD) and a magnifying lens assembly. Images captured using such a sensor and magnifying lens assembly are generally polluted by systematic distortions referred to as radial and tangential distortions (Slama, 1980). If a subset moves across a significant proportion of the image width, these distortions can lead to significant measurement errors. In addition, differential movement of the camera and model during the experiment, such as that observed during centrifuge ramp-up by White *et al.* (2003), can lead to further measurement errors. Mathematical models for these distortions and movements have been developed to correct and scale the PIV/DIC displacement measurements in a process known as close-range

photogrammetry (e.g. Heikkilä, 2000; Pan *et al.*, 2013; Soloff *et al.*, 1997; White *et al.*, 2003).

Close-range photogrammetry generally requires at least 12 static control points – of known image space (typically determined by centroiding) and object space location (measured or prescribed in manufacture) – distributed uniformly across the image, in order to solve the mathematical models for the lens distortions and camera-model movements (rotations and translations) simultaneously by minimising the difference between the modelled and known control point locations. Figure 3 shows that the apparatus described in this paper has adequate control points in the 'macro' FoV; however, only four control points are visible in the 'micro' FoV. Hence, to minimise the area of the soil sample obscured by static control points, the authors preferred not to machine additional static control points into the transparent window of the strongbox. Instead an alternative photogrammetric correction process has been developed and validated for the 'micro' FoV analysis.

5.2 Methodology

The photogrammetric correction method utilised in this paper is based on that described by White *et al.* (2003). It consists of

International Journal of Physical Modelling in Geotechnics
Volume 17 Issue 1

**Synchronised multi-scale image analysis
of soil deformations**
Teng, Stanier and Gourvenec
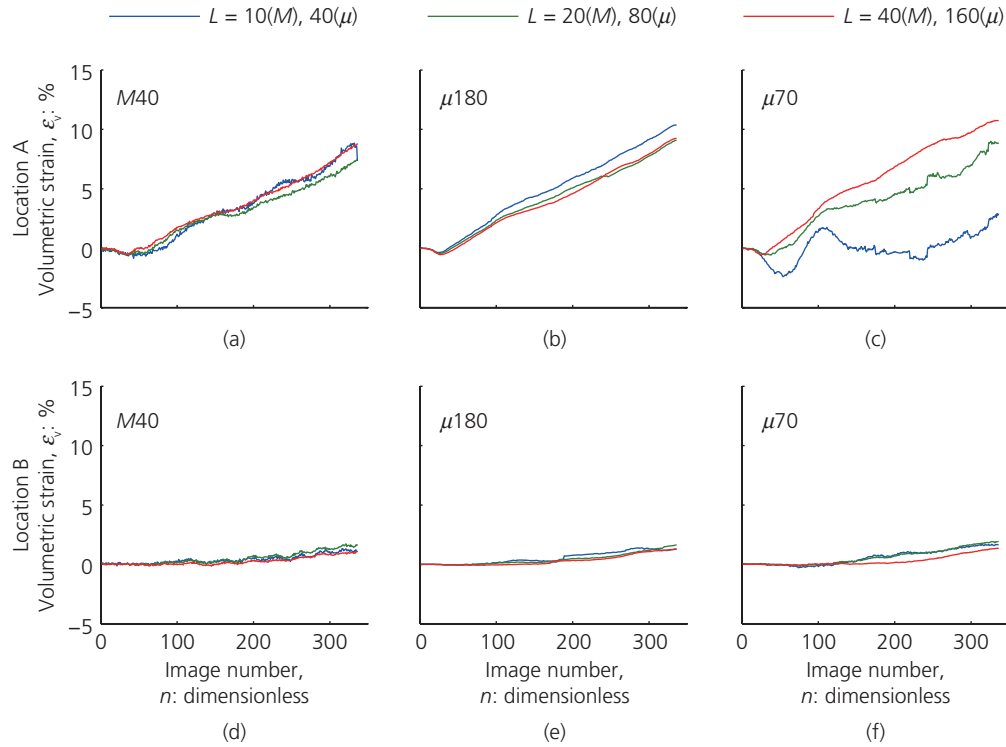
Figure 8. Volumetric strain (ε_v) measured using triangular elements of varying element length L at locations A and B for: (a, d) 40-pixel diameter subset in 'macro' view ($M40$); (b, e) 180-pixel diameter subset in 'micro' view ($\mu180$); and (c, f) 70-pixel diameter subset in 'micro' view ($\mu70$)

a pinhole camera model (illustrated in Figure 10) to account for camera-model differential movement (rotations and translations) incorporating functions to correct for four sources of camera-lens-induced distortion including: the CCD-model non-parallelism, radial distortion, tangential distortion and pixel non-squareness. The equation used to derive object space coordinates (X, Y) from distortion-corrected image space coordinates (x_c, y_c) is as follows

3.
$$\begin{bmatrix} \mu X \\ \mu Y \\ \mu \end{bmatrix} = \mathbf{P_R}^{-1}\mathbf{P_P}^{-1}\mathbf{P_C}^{-1} \begin{bmatrix} x_c \\ y_c \\ 1 \end{bmatrix}$$
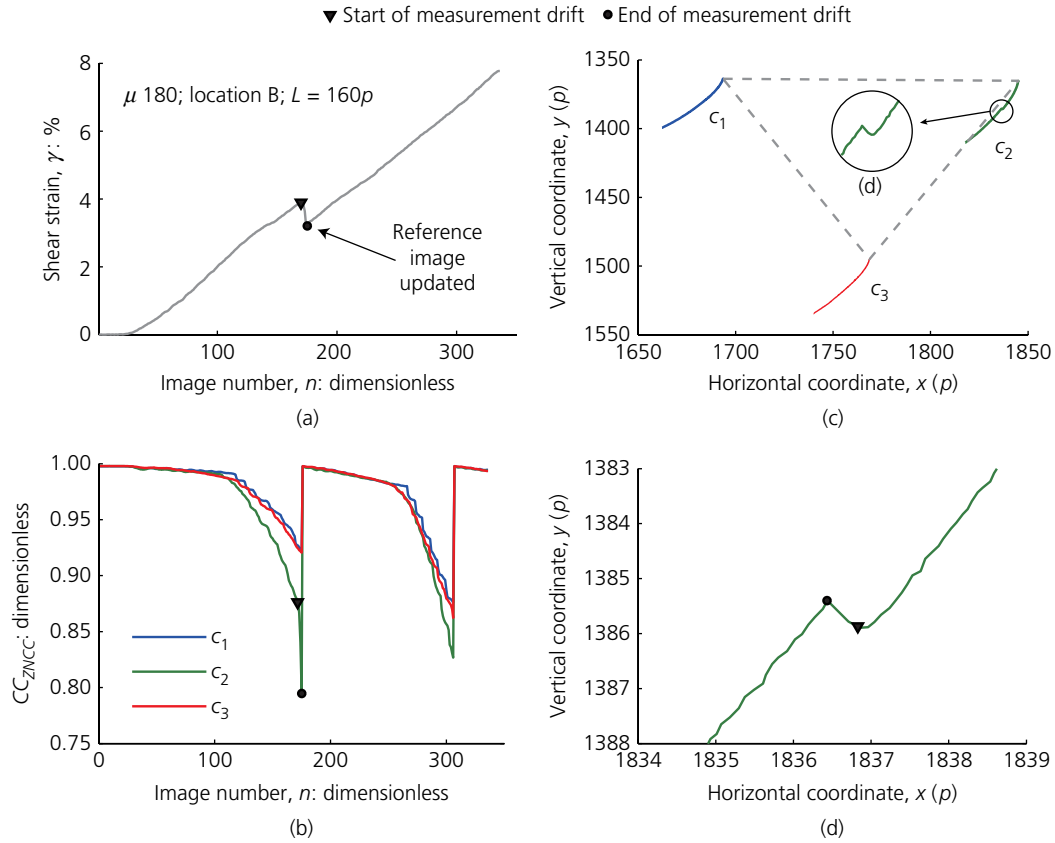
where μ is a pixel coordinate scale factor and the matrices $\mathbf{P_R}$, $\mathbf{P_C}$ and $\mathbf{P_P}$ are the rotation and translation, camera calibration and the perspective project matrices, respectively, which are defined as follows.

4.
$$\mathbf{P_R} = \begin{bmatrix} r_{11} & r_{12} & t_x \\ r_{21} & r_{22} & t_y \\ r_{31} & r_{32} & t_z \end{bmatrix}$$

5.
$$\begin{aligned} r_{11} &= \cos\phi\cos\kappa \\ r_{12} &= -\sin\kappa\cos\omega + \cos\kappa\sin\phi\sin\omega \\ r_{21} &= \sin\kappa\cos\phi \\ r_{22} &= \cos\kappa\cos\omega + \sin\kappa\sin\phi\sin\omega \\ r_{31} &= -\sin\phi \\ r_{32} &= \cos\phi\sin\omega \end{aligned}$$

6.
$$\mathbf{P_C} = \begin{bmatrix} \dfrac{1}{D_x} & 0 & x_0 \\ 0 & \dfrac{1}{D_y} & y_0 \\ 0 & 0 & 1 \end{bmatrix}$$

7.
$$\mathbf{P_P} = \begin{bmatrix} f & 0 & 0 \\ 0 & f & 0 \\ 0 & 0 & 1 \end{bmatrix}$$

International Journal of Physical Modelling in Geotechnics
Volume 17 Issue 1

Synchronised multi-scale image analysis
of soil deformations
Teng, Stanier and Gourvenec

▼ Start of measurement drift ● End of measurement drift

Figure 9. Effect of subset shape function mismatch on strain computations: (a) sudden shear strain drift caused by (b) sudden decorrelation due to subset shape function mismatch immediately prior to 'reference' image updating, resulting in (c, d) erroneous displacement measurement drift, which pollutes the strain computations

The distortion-corrected image space coordinates (x_c, y_c) are derived from the image space coordinates (x, y) as follows

8.
$$\begin{bmatrix} x_c \\ y_c \end{bmatrix} = \begin{bmatrix} (\tilde{x} + \delta_{\tilde{x}:r} + \delta_{\tilde{x}:t}) \dfrac{1}{D_x} \\ (\tilde{y} + \delta_{\tilde{y}:r} + \delta_{\tilde{y}:t}) \dfrac{1}{D_y} \end{bmatrix}$$

9.
$$\begin{bmatrix} \delta_{\tilde{x}:t} \\ \delta_{\tilde{y}:t} \end{bmatrix} = \begin{bmatrix} 2p_1 \tilde{x}\tilde{y} + p_2 (r^2 + 2\tilde{x}^2) \\ p_1 (r^2 + 2\tilde{y}^2) + 2p_2 \tilde{x}\tilde{y} \end{bmatrix}$$

10.
$$\begin{bmatrix} \delta_{\tilde{x}:r} \\ \delta_{\tilde{y}:r} \end{bmatrix} = \begin{bmatrix} \tilde{x}(k_1 r^2 + k_2 r^4) \\ \tilde{y}(k_1 r^2 + k_2 r^4) \end{bmatrix}$$

11.
$$\begin{bmatrix} \tilde{x} \\ \tilde{y} \end{bmatrix} = \begin{bmatrix} (x - x_0)D_x \\ (y - y_0)D_y \end{bmatrix}$$

12.
$$r = \sqrt{\tilde{x}^2 + \tilde{y}^2}$$

The coordinate scale factor μ in Equation 3 exists because there is no single solution for the transformation of two-dimensional (2D) image space coordinates to three-dimensional object space coordinates; similar but scaled objects appear the same along the optical axis (White, 2002). Therefore, since only measurements on a plane (against the transparent window of the strongbox) are required to be converted from 2D image space coordinates (x, y) to 2D object space coordinates (X, Y), the magnitude of μ is derived as a product of matrix multiplication and cancels through division.

63

Transformation of x,y to X,Y performed using Equations 3–11:

$$x, y \rightarrow X, Y = f\,(f,\ \alpha\,(=D_y/D_x),\ x_0,\ y_0,\ k_1,\ k_2,\ p_1,\ p_2,\ \omega,\ \phi,\ \kappa,\ t_x,\ t_y,\ t_z)$$

Camera calibration parameters   Rotation and translation parameters
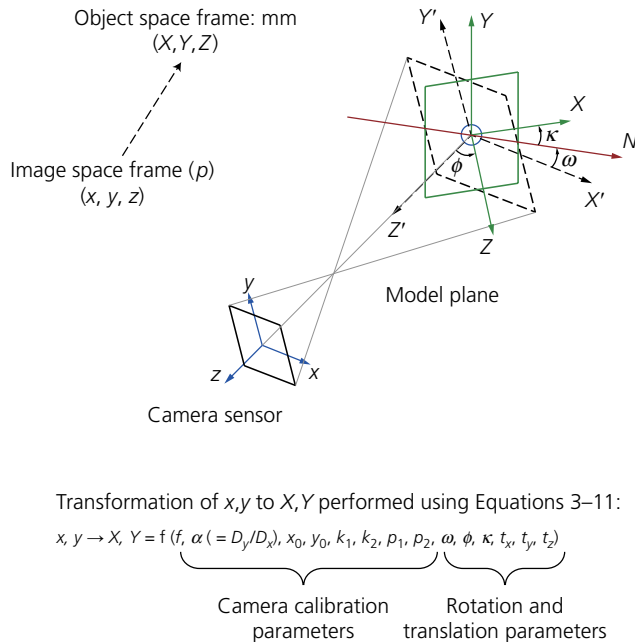
Figure 10. Pinhole camera model for converting image space measurements (x, y) to object space measurements (X, Y)

Therefore, the photogrammetric system has 14 remaining unknowns that must be optimised for each 'reference' and 'target' image pair. These parameters can be separated into two categories.

- Camera calibration parameters determined by calibration of the imaging hardware: focal length (f), principal point (x_0, y_0), radial lens distortion parameters (k_1, k_2), tangential lens distortion parameters (p_1, p_2) and CCD non-squareness ratio $(\alpha = D_y/D_x$, where D_x and D_y are the dimensions of a pixel on the sensor in object space units).
- Rotation and translation parameters describing the relative position of the camera sensor and model plane: three Euler rotational angles (ω, ϕ, κ) and three translation magnitudes (t_x, t_y, t_z).

Typically, all 14 unknowns are optimised simultaneously by minimising the error between the measured and known coordinates of the static control points. However, this direct one-step approach is not possible for the 'micro' FoV where only four static control points are visible. Instead, the authors propose to pre-calibrate the camera-lens calibration parameters, fixing eight of the 14 unknowns throughout the experiment. The displacement of the four control points is then used to determine the rotation and translation parameters through optimisation. This alternative process is summarised by the flowchart in Figure 11. The validity of the approach relies on

the assumption that

- the nature of the camera-lens-induced distortions does not change during the experiment (very unlikely for $1\boldsymbol{g}$ tests but potentially problematic for centrifuge modelling where the lens assembly is subjected to higher stresses)
- the rotation and translation parameters can be adequately optimised using displacements of only four static control points.

The following validation will demonstrate that the above assumptions are reasonable even for centrifuge model tests.
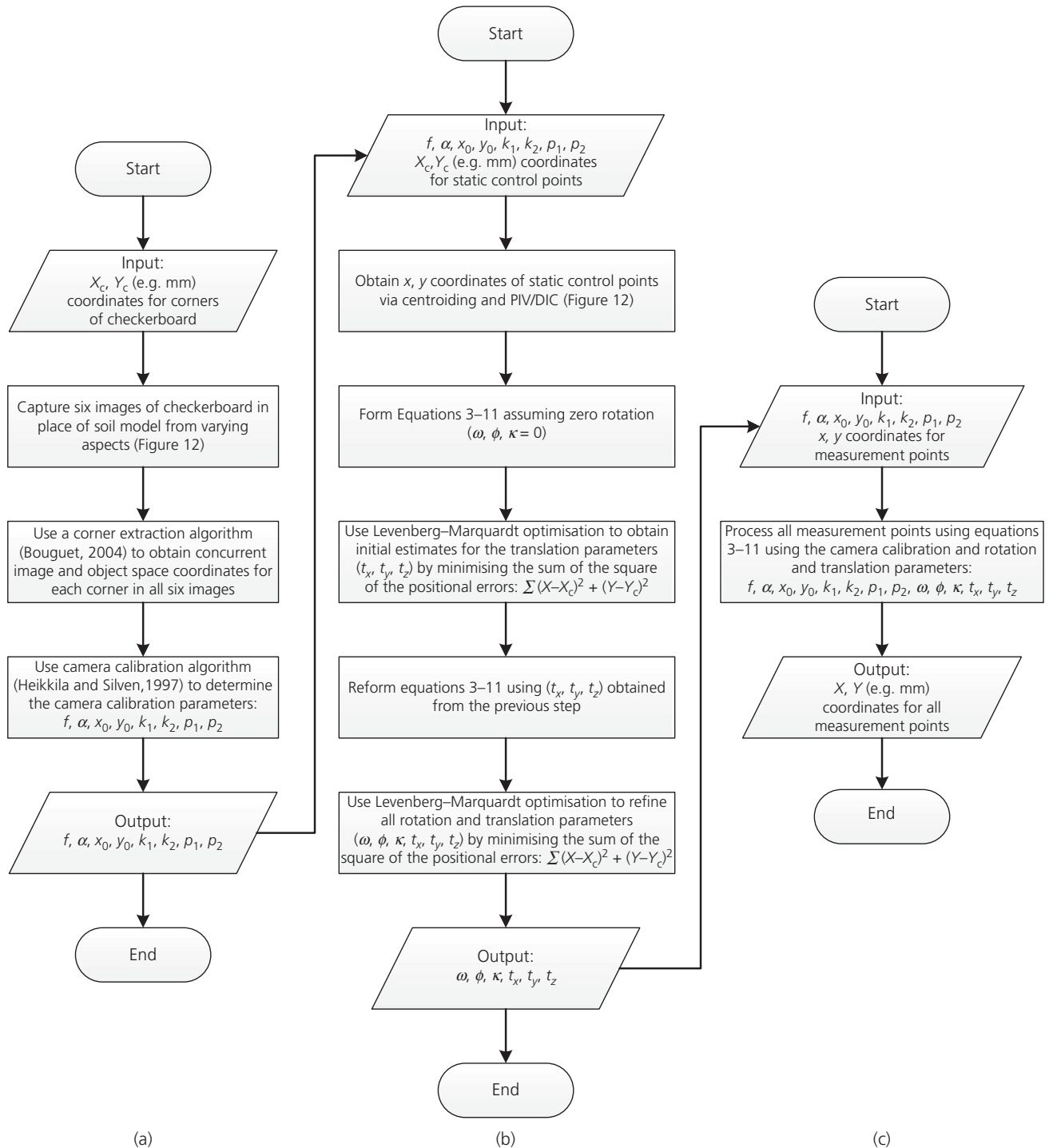
5.3 Pre-calibration

The camera calibration parameters $(f, x_0, y_0, k_1, k_2, p_1, p_2$ and $\alpha)$ were derived using six digital images of a black and white checkerboard that was located in place of the soil sample shown in Figure 2, as illustrated in Figure 12. Each of the images was captured from a slightly different aspect by inclining the checkerboard. The image space coordinates of each of the squares of the checkerboard (48 in total) were extracted using a corner extraction algorithm (Bouguet, 2004), as shown for one of the six calibration images in Figure 12(b). The object space coordinates were specified when printing the checkerboard. These concurrent image and object space coordinates for the six images were then input into a camera calibration algorithm (Heikkilä and Silvén, 1997) to identify the camera calibration parameters and assumed to remain constant throughout the experiment.

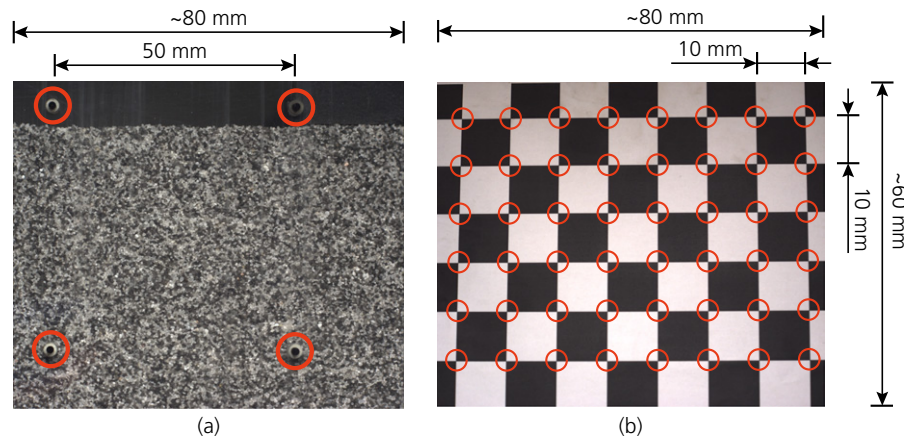### 5.4 Rotation and translation parameter optimisation

The remaining six unknowns in the system of photogrammetric equations (three Euler rotational angles, ω, ϕ and κ; and three translation magnitudes, t_x, t_y and t_z) were optimised for each 'reference' and 'target' image pair using the Levenberg–Marquardt least-square fitting algorithm (Moré, 1978) as summarised in the flowchart in Figure 11. The optimisation of the six unknowns was conducted in two steps.

- First, since the camera was aligned with the model so that the sensor was parallel with the model plane, and the relative rotation of the camera and model was expected to be small, the rotation angles, ω, ϕ and κ, were assumed to be zero so as to obtain initial estimates of the translation magnitudes, t_x, t_y and t_z that are close to the optimal solution.
- Second, all six unknowns are refined using the initial estimates for t_x, t_y and t_z to precondition the system of equations.

This preconditioning process leads to faster and more reliable optimisation of the six image–object space transformation

64

International Journal of Physical Modelling in Geotechnics
Volume 17 Issue 1

Synchronised multi-scale image analysis
of soil deformations
Teng, Stanier and Gourvenec

Figure 11. Flowchart detailing the steps involved in the proposed
pre-calibrated photogrammetric correction process: (a) camera
calibration; (b) rotation and translation parameter optimisation;
and (c) measurement point processing

International Journal of Physical Modelling in Geotechnics
Volume 17 Issue 1

Synchronised multi-scale image analysis
of soil deformations
Teng, Stanier and Gourvenec

Figure 12. Pre-calibration of the camera calibration parameters using a checkerboard in place of the soil sample and corner extraction: (a) 'micro' view of soil sample with four static control points circled; and (b) checkerboard used in place of soil sample during calibration with corners circled

parameters. In cases where the camera sensor is non-parallel with the model plane, as might be apparent in some experimental set-ups where the camera cannot be aligned to view the model plane head on, estimates of the initial angles could be used to precondition the system of photogrammetric equations in lieu of the null values the authors have assumed.

5.5 Validation

To validate the above approach, images captured during centrifuge ramp-up by the 'macro' view camera, in which 30 static control points were visible, were used to compare the conventional photogrammetric correction process of White *et al.* (2003) with the proposed pre-calibrated approach. Groups of four control points with varying spacing and position were identified in the 'macro' view images, with the control points with the largest spacing in the 'macro' FoV being in broadly the same image space location as the four control points visible in the 'micro' FoV, as illustrated in Figure 13(a). The measured (by way of centroiding) image and known object space (measured) coordinates of these groups of four control points were then used in the rotation and translation parameter optimisation process to determine the six remaining unknowns (ω, ϕ, κ, t_x, t_y and t_z), from which the coordinates of the remaining 26 static control points were predicted. The standard deviation of the positional errors (the difference between known and predicted locations) was then calculated throughout the image series for each grouping, as shown in Figure 13(b), plotted against centrifuge acceleration. These results lead to the following conclusions.

- The pre-calibrated approach is only slightly less precise than the conventional approach (which has six times the

input data available for use in the camera calibration parameter optimisation process).
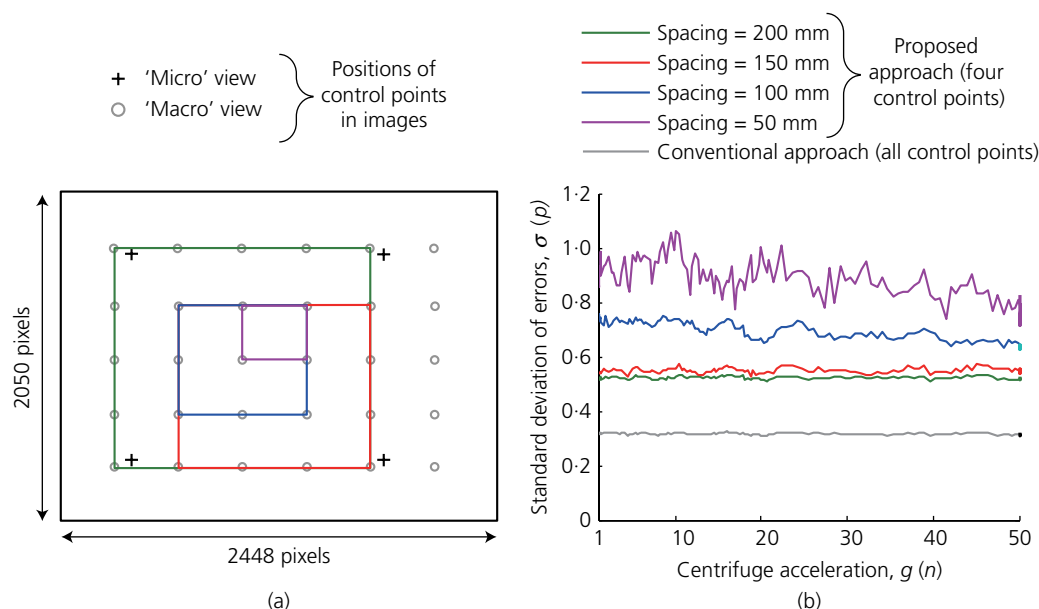- The precision of the pre-calibrated approach is stable throughout the experiment for control point spacing similar to that used in the 'micro' view set-up. This indicates that the assumption that the camera-lens distortion parameters can be assumed to remain constant – even during a centrifuge test – is reasonable.
- The closer the four control points are to each other, the higher the precision degradation. Therefore, where only a small number of control points are visible, images should be captured such that the control points are in the periphery of the FoV.

The modest reduction in precision (in image space terms) between the conventional approach and the proposed pre-calibrated approach is insignificant compared with the gains in measurement resolution that are realised by the use of the 'micro' view camera, as demonstrated in the example below. The four-fold reduction in FoV results in object space positional precision in the 'micro' view images that is actually better than that in the 'macro' view, for the control point locations adopted in the authors' apparatus.

6. Example strain field measurements

The spatial shear and volumetric strain fields generated during the first $0.01B$ of footing settlement are plotted in Figures 14 and 15, respectively, for both image scales ('macro' and 'micro') and a variety of subset sizes and spacings. For all these analyses, the seed correlation coefficient tolerance ($CC_{ZNCC\text{-}seed\text{-}tol}$; Stanier *et al.*, 2015) was set as 0.9 while all other analysis parameters were as defined earlier.

International Journal of Physical Modelling in Geotechnics
Volume 17 Issue 1

Synchronised multi-scale image analysis
of soil deformations
Teng, Stanier and Gourvenec

Figure 13. Pre-calibrated photogrammetric correction validation: (a) location of sets of four control points in the 'macro' view images used in the validation process compared with the locations of those available in the ana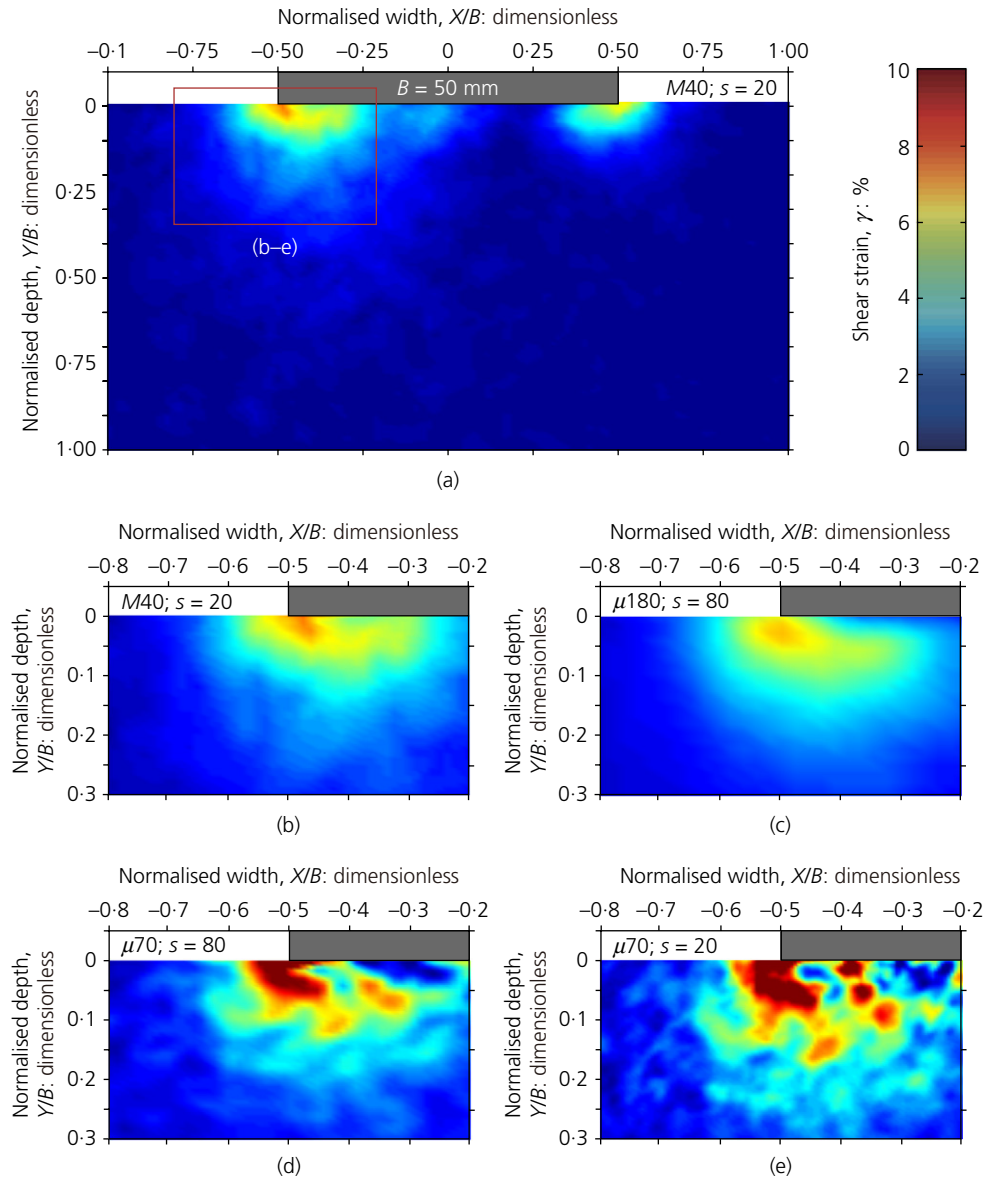lysis of the 'micro' view images; and (b) precision of the proposed pre-calibrated photogrammetric correction process compared with the conventional approach during centrifuge ramp-up

Figures 14 and 15(a) show the full shear and volumetric strain fields observed by the 'macro' view camera, analysed using a 40-pixel diameter subset ($M40$; $D_s = 40p$) with 20-pixel regular grid spacing ($s = 20p$). Figures 14 and 15(b) show a zoomed region of the same 'macro' FoV analysis that is equivalent to the region of the model viewed by the 'micro' FoV. Figures 14 and 15(c) present the results of an analysis of the 'micro' FoV images using 180-pixel diameter subsets ($\mu180$; $D_s = 180p$) at approximately the same object space spacing as the 'macro' view analysis ($s = 80p$). Comparing Figures 14 and 15(b) and 15(c) show that the 'macro' and 'micro' FoV analyses with equivalent object space subset size and spacing result in very similar strain fields. However, the 'reference' image had to be updated more regularly for the 'micro' FoV analysis due to the periodic rapid decorrelation caused by the subset shape function becoming 'under-matched'. This indicates that the higher resolution ($d/p \approx 18$) 'micro' view camera is capturing details of the deformation processes that are not captured by the comparatively lower resolution ($d/p \approx 4$) 'macro' view images and that the large subset size precludes their measurement.

Figures 14 and 15(d) show the effect of reducing the subset size to 70 pixels ($\mu70$; $D_s = 70p$) in the 'micro' FoV analysis, while keeping the subset spacing the same ($s = 80p$). Immediately beneath the footing a thin band ($\sim0.06B$) of

dilating material is observed in Figure 15(d), which was not captured by the analyses in Figures 15(b) and 15(c). The smaller ($\mu70$) subset is of the order of $\sim0.04B$ in size, so the subsets are small enough to populate the dilating feature. In contrast, the larger ($M40$ and $\mu180$) subsets are of the order of $\sim0.1B$ in size, which is significantly larger than the feature observed. This results in subsets straddling the feature, precluding accurate measurement of the deformations occurring within it due to the subset shape becoming 'under-matched'. The smaller subsets are better able to match the deformation within the feature, resulting in less frequent 'reference' image updating and accurate measurement of deformation.

Lastly, Figures 14 and 15(e) show the effect of using the same small subset size ($\mu70$) but with reduced spacing ($s = 20p$), which results in a 16-fold increase in measurement density. Stanier et al. (2016) demonstrated that bias errors manifest themselves in strain fields by amplifying the strain magnitudes in proportion to the reduction in subset spacing (i.e. strain element gauge length). In this case, the same general features and strain magnitudes shown in Figures 14 and 15(d) are evident, providing confidence that the measurements are not affected by such bias errors. The closer subset spacing results in strain element sizes much smaller than the strain features being observed in the experiment, yielding comparatively more detailed strain fields than the analysis with larger
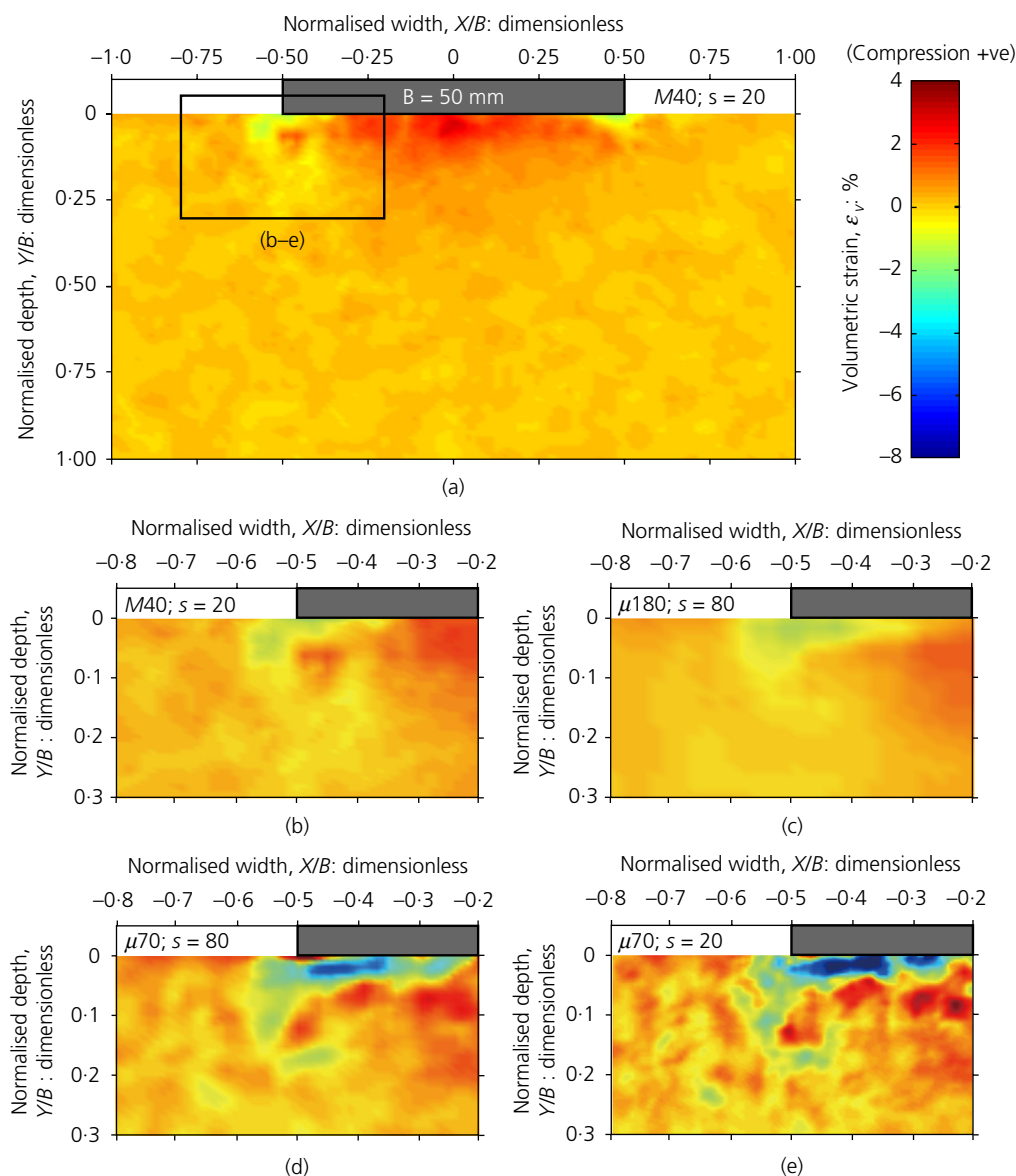
67

International Journal of Physical Modelling in Geotechnics
Volume 17 Issue 1

**Synchronised multi-scale image analysis
of soil deformations**
Teng, Stanier and Gourvenec

Figure 14. Shear strain fields (γ) beneath a strip footing penetrating into dense silica sand: (a) 'macro' view for $D_s = 40p$; $s = 20p$; (b) zoomed region of 'macro' view equivalent to 'micro' view; (c) 'micro' view for $D_s = 180p$; $s = 80p$; (d) 'micro' view for $D_s = 70p$; $s = 80p$; and (e) 'micro' view for $D_s = 70p$; $s = 20p$

subset spacing (c.f. Figures 14(d), 14(e), 15(d) and 15(e)). This analysis confirms that for this experimental set-up and granular material, the optimum subset size is ~ 70 pixels and the subset spacing is ~ 20 pixels.

For different experimental set-ups and soils it is recommended to determine carefully appropriate subset sizes by: (a) assessing the subset texture quality for a wide range of subset sizes and (b) exploring the effect of subset spacing (i.e. strain element

gauge length) on strain measurements that are derived from the displacement fields. The use of higher resolution images ($d/p \gg 4$), the smallest subset size exhibiting adequate image texture quality and close spacing results in the ability to observe small localised strain features that are either not captured by low-resolution images ($d/p \approx 4$) or are masked by the subset shape function becoming 'under-matched' in the analyses performed on high-resolution images ($d/p \approx 18$) using subsets that are larger than necessary.

International Journal of Physical Modelling in Geotechnics
Volume 17 Issue 1

**Synchronised multi-scale image analysis
of soil deformations**
Teng, Stanier and Gourvenec

Figure 15. Volumetric strain fields (ε_v) beneath a strip footing penetrating into dense silica sand: (a) 'macro' view for $D_s = 40p$; $s = 20p$; (b) zoomed region of 'macro' view equivalent to 'micro' view; (c) 'micro' view for $D_s = 180p$; $s = 80p$; (d) 'micro' view for $D_s = 70p$; $s = 80p$; and (e) 'micro' view for $D_s = 70p$; $s = 20p$

7.   Conclusions

A multi-scale image analysis system has been described that can capture images of 'macro' failure mechanism and 'micro' scale deformation localisations using a pair of synchronously triggered digital cameras viewing different regions of a geotechnical model test. The hardware and software required for such a system has been described. Guidance has been given on the appropriate choice of analysis parameters, including subset size and spacing. Pitfalls caused by inappropriate choice of those user-defined analysis parameters have been described and demonstrated using example data from a centrifuge test modelling the settlement of a strip footing on silica sand. A modified photogrammetric correction procedure to convert image space (pixel) measurements to model units (e.g. mm) – requiring as few as four static control points to be visible within the images being analysed – has been proposed. This procedure has been validated using images obtained during

69

International Journal of Physical Modelling in Geotechnics
Volume 17 Issue 1

Synchronised multi-scale image analysis
of soil deformations
Teng, Stanier and Gourvenec

centrifuge ramp-up, illustrating that it is reasonable to assume that camera calibration parameters can remain constant throughout an experiment with minimal loss of positional accuracy and precision. Lastly, the effect of image scale, subset size and spacing on strain field measurements has been demonstrated. High-resolution ($d/p \approx 18$) images that are analysed using the smallest subset exhibiting adequate image texture quality measures and close spacing result in highly detailed strain fields that are either not captured by low-resolution images ($d/p \approx 4$) or are masked in the analyses of high-resolution images that utilise subsets that are larger than necessary.

Acknowledgements

REFERENCES

Adrian RJ (1991) Particle-imaging techniques for experimental fluid mechanics. *Annual Review of Fluid Mechanics* **23(1)**: 261–304.

Anastasopoulos I, Gazetas M, Bransby M, Davies M and El Nahas A (2007) Fault rupture propagation through sand: finite-element analysis and validation through centrifuge experiments. *Journal of Geotechnical and Geoenvironmental Engineeering* **133(8)**: 943–958.

Avril S, Bonnet M, Brettelle AS *et al.* (2008) Overview of identification methods of mechanical parameters based on full-field measurements. *Experimental Mechanics* **48**: 381–402.

Blaber J, Adair B and Antoniou A (2015). Ncorr: open-source 2D digital image correlation matlab software. *Experimental Mechanics* **55(6)**: 1105–1122.

Bouguet JY (2004) *Camera Calibration Toolbox for Matlab*. See http://www.vision.caltech.edu/bouguetj/calib_doc (accessed 29/06/2016).

Cheng P, Sutton MA, Schreier HW and McNeill SR (2002) Full field speckle pattern image correlation with b-spline deformation function. *Experimental Mechanics* **42(3)**: 344–352.

Dingle HRC, White DJ and Gaudin C (2008) Mechanisms of pipe embedment and lateral breakout on soft clay. *Canadian Geotechnical Journal* **45(5)**: 636–652.

Hall S (2012) Digital image correlation in experimental geomechanics. *ALERT Geomaterials Doctoral Summer School 2012, Aussois, France*. ALERT Geomaterials, pp. 69–102.

Heikkilä J (2000) Geometric camera calibration using circular control points. *IEEE Transactions on Pattern Analysis and Machine Intelligence* **22(10)**: 1066–1077.

Heikkilä J and Silvén O (1997) A four-step camera calibration procedure with implicit image correction. *Proceedings of the 1997 IEEE Computer Society Conference on Computer Vision and Pattern Recognition, San Juan, CA, USA*. IEEE, pp. 1106–1112.

Hu P, Wang D, Cassidy MJ and Stanier SA (2014) Assessing the punch-through hazard of a spudcan on sand overlying clay. *Géotechnique* **65(11)**: 1–14, http://dx.doi.org/10.1680/jgeot.14.P.097.

Iskander M (2010) *Modelling with Transparent Soils*. Springer, Berlin, Germany.

Lewis JP (1995). *Fast normalized cross-correlation*. Vision interface, Quebec, QC, Canada.

Mana DSK, Gourvenec S and Martin CM (2012) Critical skirt spacing for shallow foundations under general loading. *Journal of Geotechnical and Geoenvironmental Engineering* **139(9)**: 1554–1566.

Marshall A, Farrel R, Klar A and Mair R (2012) Tunnels in sands: the effect of size, depth and volume loss on greenfield displacements. *Géotechnique* **62(5)**: 385–399, http://dx.doi.org/10.1680/geot.10.P.047.

Moré JJ (1978) The Levenberg–Marquardt algorithm: implementation and theory. In *Numerical Analysis* (Watson GA (ed.)), Springer, Argonne, IL, USA, pp. 105–116.

Muir Wood DM (2012) Heterogeneity and soil element testing. *Géotechnique Letters* **2**: 101–106, http://dx.doi.org/10.1680/geolett.12.00019.

Omidvar M, Chen Z and Iskander M (2014) Image-base Lagrangian analysis of granular kinematics. *Journal of Computing in Civil Engineering* **29(6)**: 1–16.

Pan B, Xie H, Wang Z, Qian K and Wang Z (2008) Study on subset size selection in digital image correlation for speckle patterns. *Optics Express* **16(10)**: 7037–7048.

Pan B, Xie H and Wang Z (2010) Equivalence of digital image correlation criteria for pattern matching. *Applied Optics* **49(28)**: 5501–5509.

Pan B, Yu L, Wu D and Tang L (2013) Systematic errors in two-dimensional digital image correlation due to lens

International Journal of Physical Modelling in Geotechnics
Volume 17 Issue 1

Synchronised multi-scale image analysis
of soil deformations
Teng, Stanier and Gourvenec

distortion. *Optics and Lasers in Engineering* **51(2)**:
140–147.

Rechenmacher AL and Finno RJ (2004) Digital image
correlation to evaluate shear banding in dilative sands.
ASTM Geotechnical Testing Journal **27(1)**: 13–22.

Schreier HW and Sutton MA (2002) Systematic errors in
digital image correlation due to under matched subset
shape functions. *Experimental Mechanics* **42(3)**: 303–310.

Slama C (1980) *Manual of Photogrammetry*, 4th edn. American
Society of Photogrammetry, Falls Church, VA, USA.

Soloff SM, Adrian RJ and Liu ZC (1997) Distortion
compensation for generalized stereoscopic particle image
velocimetry. *Measurement Science and Technology* **8(12)**:
1441.

Stanier SA and White DJ (2013) Improved image-based
deformation measurement in the centrifuge environment.
Geotechnical Testing Journal **36(6)**: 1–14.

Stanier SA, Black JA and Hird CC (2013) Modelling helical screw
piles in soft clay and design implications. *Proceedings of
the Institution of Civil Engineers – Geotechnical
Engineering* **167(5)**: 447–460, http://dx.doi.
org/10.1680/geng.13.00021.

Stanier SA, Blaber J, Take W and White D (2015) Improved
image-based deformation measurement for geotechnical
applications. *Canadian Geotechnical Journal* **53(5)**:
727–739.

Stanier SA, Dijkstra J, Leśniewska D et al. (2016) Vermiculate
artefacts in image analysis of granular materials.
Computers and Geotechnics **72**: 100–113.

Sutton MA, Wolters WJ, Peters WH, Ranson WF and McNeill SR
(1983) Determination of displacements using an improved
digital correlation method. *Image and Vision Computing*
1(3): 133–139.

Sutton MA, McNeill SR, Helm JD and Chao YJ (2000)
*Advances in Two-Dimensional and Three-Dimensional
Computer Vision Photomechanics*. Springer,
pp. 323–372.

Take WA (2015) Thirty-sixth Canadian geotechnical
colloquium: advances in visualization of geotechnical
processes through digital image correlation. *Canadian
Geotechnical Journal* **52(9)**: 1199–1220.

Take W and Bolton M (2011) Seasonal ratcheting and softening
in clay slopes, leading to first-time failure. *Géotechnique*
61(9): 757–769, http://dx.doi.org/10.1680/geot.9.P.125.

Westerweel J (1997) Fundamentals of digital particle image
velocimetry. *Measurement Science and Technology* **8(12)**:
1379.

White D (2002) *An Investigation into the Behaviour of
Pressed-In Piles*. PhD thesis, University of Cambridge,
Cambridge, UK.

White DJ and Bolton MD (2004) Displacement and strain paths
during plane-strain model pile installation in sand.
Geotechnique **54(6)**: 375–397, http://dx.doi.org/
10.1680/geot.2004.54.6.375.

White DJ, Take WA, Bolton MD and Munachen SE (2001) A
deformation measuring system for geotechnical testing
based on digital imaging, close-range photogrammetry,
and PIV image analysis. *Proceedings of the 15th
International Conference on Soil Mechanics and
Geotechnical Engineering, Istanbul, Turkey*
(Anagnostopoulos A, Pachakis M and Tsatsanifos C (eds)).
Balkema, Rotterdam, the Netherlands, pp. 539–542.

White DJ, Take WA and Bolton MD (2003) Soil deformation
measurement using particle image velocimetry (PIV) and
photogrammetry. *Geotechnique* **53(7)**: 619–631, http://dx.
doi.org/10.1680/geot.2003.53.7.619.